

Simulation study of the harmonic structure of lower hybrid waves driven by energetic ions

Tsubasa Kotani ^{1,*}, Mieko Toida ², Toseo Moritaka ², and Satoshi Taguchi ¹

¹Graduate School of Science, Kyoto University, Kyoto 606-8502, Japan

²National Institute for Fusion Science, Toki, Gifu 509-5202, Japan

 (Received 29 August 2022; revised 7 June 2023; accepted 1 August 2023; published 15 September 2023)

By means of one-dimensional, electromagnetic, particle-in-cell simulations considering the effects of energetic-ion injection, we study the harmonic structure of lower hybrid waves (LHWs) driven by energetic ions under the condition where the electron plasma frequency (ω_{pe}) is smaller than the electron cyclotron frequency (Ω_e). It is found that after the LHWs are excited with the wave number and frequency of (k_1, ω_1) , many harmonic LHWs are generated at $(mk_1, n\omega_1)$ where m and n are integers, up to far beyond the lower hybrid resonance frequency, m and $n \sim 10$. We show that the harmonic LHWs are generated by nonlinear wave-wave coupling between the LHWs directly excited by the energetic ions and the energetic-ion cyclotron waves above the lower hybrid resonance frequency. We also find that the harmonic LHWs can exist even after the energetic ions are artificially removed because they can be coupled with ion Bernstein waves due to bulk ions. The effect of the energetic-ion injection and the dependence of ω_{pe}/Ω_e on the development of the harmonic LHWs are investigated to compare the simulation results with an observation in Earth's magnetosphere.

DOI: [10.1103/PhysRevE.108.035208](https://doi.org/10.1103/PhysRevE.108.035208)

I. INTRODUCTION

Based on cold plasma approximation, the characteristics of waves propagating perpendicular to the magnetic field are completely different below and above the lower hybrid resonance frequency (ω_{LH}) defined as

$$\omega_{LH}^2 = (\Omega_i \Omega_e)^2 \frac{1 + \omega_{pi}^2 / \Omega_i^2}{\omega_{pe}^2 + \Omega_e^2}. \quad (1)$$

Here, the subscript s denotes particle species ($s = i$ and $s = e$), Ω_s is the cyclotron frequency, and ω_{ps} is the plasma frequency. Below ω_{LH} , there is a dispersion branch of $\omega = kv_A$ in the limit of $k \rightarrow 0$, where v_A is the Alfvén speed, and $\omega = \omega_{LH}$ in the limit of $k \rightarrow \infty$. This branch corresponds to magnetosonic and lower hybrid waves. The magnetosonic wave in the small-wave-number region is almost electromagnetic, whereas the lower hybrid wave in the large-wave-number region is almost electrostatic. However, above ω_{LH} , there is no dispersion branch and waves are evanescent. This means that wave excitation is much more difficult above ω_{LH} than below it even if plasma kinetic effects are considered [1]. In this paper, we study the excitation and development of such unusual waves above ω_{LH} caused by nonlinear wave-wave coupling due to lower hybrid waves (LHWs) driven by energetic ions.

The LHWs are observed in various plasma environments such as comet [2], fusion [3,4], and magnetospheric plasmas [5]. In Earth's magnetosphere, the LHWs play important roles

in particle acceleration and pitch angle scattering. For example, the LHWs contribute to the energization of oxygen ions in the auroral region [6], cold ion heating in the inner magnetosphere [7,8], electron acceleration in the radiation belts [9], and the proton aurora by pitch angle scattering [10]. The mode conversion between the LHWs and whistler waves caused by density inhomogeneity has also been an important subject [11–15].

The LHWs can be excited by energetic ions with a ringlike velocity distribution perpendicular to the background magnetic field [16–21]. Suppose that the ring velocity of energetic ions is smaller than the Alfvén velocity ($v_{\perp} < v_A$), then electrostatic components are dominant in the LHWs. By contrast, electromagnetic components are dominant if the ring velocity is comparable to or larger than the Alfvén speed ($v_{\perp} \geq v_A$). The ringlike velocity distribution is observed in space and fusion plasmas. In Earth's inner magnetosphere, such distributions in both cases $v_{\perp} < v_A$ and $v_{\perp} \geq v_A$ are observed in the dusk to dayside sector associated with the excited LHWs [22].

Unlike the LHWs with $\omega \lesssim \omega_{LH}$, waves above ω_{LH} have received little attention. However, an experimental study on fusion plasma [23] has reported that unusual waves above ω_{LH} have been observed. The frequency of the unusual wave is in the range of $\omega_{LH} < \omega \lesssim 2\omega_{LH}$ and is almost twice the frequency of the dominant wave below ω_{LH} . In Ref. [23], particle-in-cell simulations were performed, and it was suggested that the unusual waves were excited by the nonlinear wave-wave coupling between these waves and ion cyclotron emissions due to fusion-born ions. In other simulation studies on energetic-ion driven instabilities [24,25], unusual waves in the range of $\omega_{LH} < \omega \lesssim 2\omega_{LH}$ were reported, although they were not investigated in detail. Other fusion experiments have reported unusual waves with $\omega > \omega_{LH}$ [26–28]. These are excited by the parametric decay instability of upper hybrid waves, and their frequencies above ω_{LH} are due to warm

*kotani@kugi.kyoto-u.ac.jp

Published by the American Physical Society under the terms of the [Creative Commons Attribution 4.0 International](https://creativecommons.org/licenses/by/4.0/) license. Further distribution of this work must maintain attribution to the author(s) and the published article's title, journal citation, and DOI.

plasma effects. Such waves with $\omega > \omega_{\text{LH}}$ have also been reported by particle-in-cell simulations [29] and investigated by a theoretical study [30].

Recently, unusual waves above ω_{LH} have been observed in Earth's magnetosphere [31]. The frequencies of the observed unusual waves are integer multiples of ω_{LH} , and the maximum frequency exceeds $2\omega_{\text{LH}}$. Here, we define these unusual waves as harmonic LHWs characterized by $\omega_n \simeq n\omega_{\text{LH}}$ where n is an integer. According to Ref. [31], the harmonic LHWs propagate almost perpendicular to the background magnetic field with linear polarization. The harmonic LHWs have larger amplitudes in the electric fields than the magnetic fields. The order of the harmonic LHWs is only up to two in the magnetic field but is up to four in the electric fields, indicating that the higher harmonic LHWs with $n = 3$ and 4 are almost electrostatic. The harmonic LHWs have been proposed to be excited by nonlinear wave-wave coupling, but the detailed excitation mechanism has not been fully understood. Also, there is a problem that energetic ions, which are believed to be necessary to excite the observed LHWs, have not been found. A particle-in-cell simulation [32] has recently found that ringlike energetic ions can generate the harmonic LHWs, but the excitation of the harmonic LHWs by nonlinear wave-wave coupling has not been confirmed.

Although there are some candidates of waves to excite the harmonic LHWs by nonlinear wave-wave coupling, they cannot explain the characteristics of the observed harmonic LHWs. For example, whistler waves, which can be generated from the LHWs due to nonlinear wave-wave coupling [19,20], cannot explain the characteristics that the harmonic LHWs propagate perpendicular to the magnetic field with dominant electrostatic components. Ion Bernstein waves due to bulk ions can interact with the LHWs; a pump LHW decays into a lower-frequency LHW and an ion Bernstein wave [33]. However, the ion Bernstein waves cannot fully explain the excitation of the harmonic LHWs because they are unlikely to be excited in the high-frequency region ($\omega > \omega_{\text{LH}}$). Although energetic-ion cyclotron waves can interact with the harmonic LHWs, the existence of such an interaction has not been confirmed. As described above, in the previous studies [23–25], the frequencies of unusual waves driven by energetic ions were reported in the range of $\omega \lesssim 2\omega_{\text{LH}}$. The nature of the higher harmonic LHWs is completely unknown.

In this paper, we use one-dimensional, electromagnetic, particle-in-cell simulations to study the excitation mechanism and development of the harmonic LHWs. We show that after the LHWs are excited directly by energetic ions, many harmonic LHWs are excited in the broadband wave-number region and the wide frequency range from 0 to far beyond $2\omega_{\text{LH}}$ by nonlinear wave-wave coupling. The higher harmonic LHWs are more electrostatic than the LHWs. This paper is organized as follows. In Sec. II, we describe the simulation methods and parameters. The two parameters, ω_{pe}/Ω_e and u_{\perp}/v_A , are chosen so that the excited LHWs are almost electrostatic. In Sec. III, we show the simulation results. The development of the harmonic LHWs and which waves are coupled with the harmonic LHWs are investigated. In Sec. IV, we discuss how the energetic-ion injection and the parameter ω_{pe}/Ω_e affect the development of the harmonic LHWs.

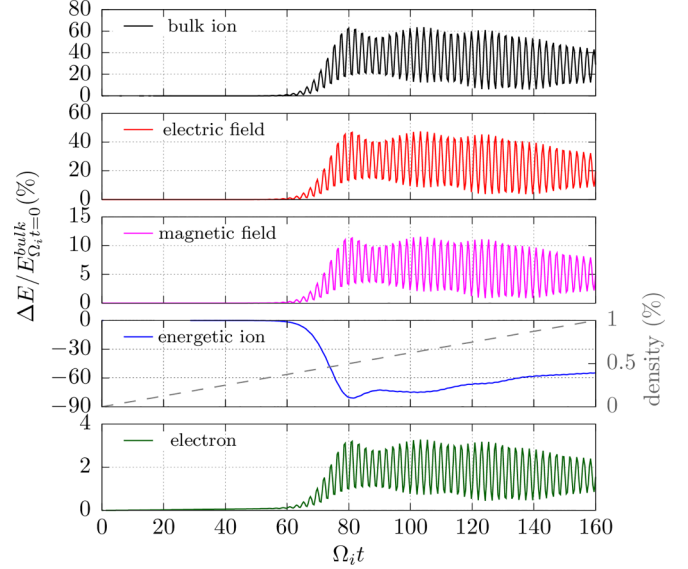


FIG. 1. Time evolution of energies for bulk ions, electric fields, magnetic fields, energetic ions, and electrons. The horizontal axis is normalized by Ω_i^{-1} . The changes from their initial values normalized by the initial energy of the bulk ions are plotted. For the energetic ions and electrons, their net energy changes are plotted. The dashed gray line in the fourth panel shows the density ratio of the energetic to bulk ions (%).

We also compare the simulation results with an observation in Earth's magnetosphere. In Sec. V, we summarize our work.

II. SIMULATION METHODS AND PARAMETERS

In this paper, we consider a plasma consisting of bulk ions, electrons, and energetic ions. We perform one-dimensional, three-velocity components electromagnetic particle-in-cell simulations with the PASTEL code [34]. To keep track of the long-term development of instabilities driven by energetic ions and wave-wave interactions, we adopt the energetic-ion injection model where the density of the energetic ions is zero at $\Omega_i t = 0$ and then gradually increases. The energetic-ion injection plays a crucial role in the development of the instabilities and the ion acceleration [25,35]. At the final step of the simulation, $\Omega_i t \simeq 160$, the density of the energetic ions is 1% to the bulk ions, which is illustrated in Fig. 1. The same number of electrons as energetic ions is also injected for charge neutrality. The positions and gyro-phases of the injected particles are given at random.

In the simulations, the initial background magnetic field and the plasma density are uniform. This is used to define the plasma parameters. The background magnetic field is along the z direction, and waves are considered to propagate in the x direction. We set a periodic boundary condition and a spatial length as $L_x = 4096\Delta$ where Δ is the grid separation equivalent to the Debye length. The time step is $0.25\Omega_e^{-1}$. The total number of computational particles is on the order of 10^8 .

We consider the following parameters. The ion-to-electron mass ratio is $m_i/m_e = 1000$, which is chosen to reduce the computational cost and to analyze waves with frequencies on

the order of Ω_i . The frequency ratio is $\omega_{pe}/\Omega_e = 0.25$, which is chosen to focus on the LHWs with dominant electrostatic components. The details are discussed below. For these parameters, the lower hybrid resonance frequency defined by Eq. (1) is $\omega_{LH} \simeq 7.7\Omega_i$. The electron beta is $\beta_e \simeq 2.0 \times 10^{-3}$. The bulk ions and electrons have Maxwellian velocity distributions with the temperature ratio $T_i/T_e = 0.2$. The electron beta and temperature ratio are arbitrarily chosen to be somewhat small such that the instabilities are not suppressed, but they are not particularly unusual compared to typical parameters of Earth's magnetosphere.

The energetic ions have a ringlike velocity distribution given by

$$f_h(v_{\perp}, v_{\parallel}) = \frac{1}{2\pi^{3/2}u_{\perp}v_{th}} \delta(v_{\perp} - u_{\perp}) \exp\left(-\frac{v_{\parallel}^2}{v_{th}^2}\right), \quad (2)$$

where the subscripts \parallel and \perp denote parallel and perpendicular to the background magnetic field, respectively, u_{\perp} is the ring speed, and v_{th} is the thermal velocity of the energetic ions. We set v_{th} equal to the thermal velocity of the bulk ions. To focus on the electrostatic LHWs, the ring speed is set to $u_{\perp} = 0.6v_A$ (v_A is the Alfvén velocity).

We consider the ratio of the electric field E_x to the magnetic field B_z . Based on the cold plasma approximation, this ratio is given by

$$\left|\frac{E_x}{B_z}\right| = \frac{v_{ph}}{c} \left|\frac{D}{S}\right|, \quad (3)$$

where v_{ph} is the phase velocity of a wave and D and S are the Stix symbols defined as [36]

$$D = \sum_s \frac{\omega_{ps}^2 \Omega_s}{\omega(\omega^2 - \Omega_s^2)}, \quad (4)$$

$$S = 1 - \sum_s \frac{\omega_{ps}^2}{\omega^2 - \Omega_s^2}. \quad (5)$$

This equation can be used to evaluate how strong the electrostatic component is relative to the electromagnetic one. When the ring velocity coincides with the phase velocity of the LHWs ($v_{ph} = u_{\perp}$), Eq. (3) is expressed as

$$\left|\frac{E_x}{B_z}\right| = \frac{u_{\perp}}{v_A} \left(\frac{m_i}{m_e}\right)^{-1/2} \left(\frac{\omega_e}{\Omega_e}\right)^{-1} \left|\frac{D}{S}\right|. \quad (6)$$

If the ratio of the ring velocity to the Alfvén velocity (u_{\perp}/v_A) is fixed, Eq. (6) is a function of the frequency ratio, ω_{pe}/Ω_e , and its value becomes the maximum for $\omega_{pe}/\Omega_e \simeq 0.25$.

When the harmonic LHWs were observed [31], energetic ions, which are believed to excite the LHWs, were not found. Therefore, we do not know the plasma parameters (such as ω_{pe}/Ω_e and u_{\perp}/v_A) needed for the simulation because the parameters at the time when the harmonic LHWs were observed may not match the ones when the harmonic LHWs were excited. ω_{pe}/Ω_e in Earth's magnetosphere takes a wide range of values. The value can be small in a region where the magnetic field is strong or the plasma density is small. Although the chosen value of ω_{pe}/Ω_e is lower than the typical one, this condition ($\omega_{pe}/\Omega_e < 1$) associated with the LHWs can exist in Earth's magnetosphere, for example, in the cusp region [37].

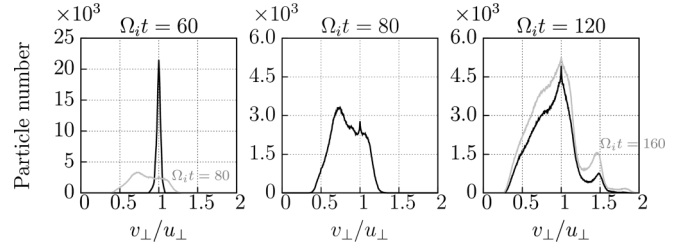


FIG. 2. Snapshots of the perpendicular velocity distribution of energetic ions at four different time points. The horizontal axis is normalized by the ring speed, u_{\perp} .

III. SIMULATION RESULTS

A. Time development of energy and velocity distribution

Before presenting the results of the harmonic structure of the LHWs, we show the time development of the velocity distribution of the energetic ions and the energy. First, we show the time evolution of total energies for bulk ions, electric and magnetic fields, energetic ions, and electrons in Fig. 1. The percentage changes from their initial values normalized by the initial bulk-ion energy are plotted. For energetic ions and electrons, the net percentage energy changes are plotted. The net change is the difference between the total energetic-ion (electron) energy at a given time t and the total injected energy of energetic ions (electrons) by the time t . Before $\Omega_i t \simeq 60$, all of the energies remain almost unchanged, which means that the instabilities driven by the ringlike energetic ions are very weak in this time interval. However, after $\Omega_i t \simeq 60$, the energetic-ion energy rapidly decreases, whereas the other energies rapidly increase. This indicates that the ringlike energetic ions excite the LHWs, which will be shown later. The excited LHWs are almost electrostatic because the electric field energy is significantly larger than the magnetic field energy. The bulk ions are accelerated by the LHWs, while the electrons are not accelerated as much. At $\Omega_i t \simeq 80$, the LHWs are saturated. After saturation, the energies of the bulk ions and electric fields maintain their large amplitudes because the newly injected energetic ions can further excite the LHWs, even after $\Omega_i t \simeq 80$. For the initial value problem, the energies of the bulk ions and electric fields significantly decrease after the saturation of the LHWs [25]. Comparison between the injection model and the initial value problem will be discussed in Sec. IV.

These results are consistent with the development of the perpendicular velocity distribution of the energetic ions. Figure 2 shows snapshots of the perpendicular velocity distribution of the energetic ions at $\Omega_i t \simeq 60, 80$, and 120 . At $\Omega_i t \simeq 60$, which is the time just before the energetic-ion energy begins to rapidly decrease (see Fig. 1), the perpendicular velocity distribution is slightly deformed from the ideal ringlike velocity distribution given by Eq. (2). At $\Omega_i t \simeq 80$, when the energetic-ion energy reaches the minimum, the perpendicular velocity distribution is drastically changed and its gradient becomes very small, as shown by the gray line in the left panel. This means that the ability to excite waves is significantly reduced due to the nonpositive or small positive gradient of the perpendicular velocity distribution. However, new energetic ions (and also electrons) are continuously injected into the

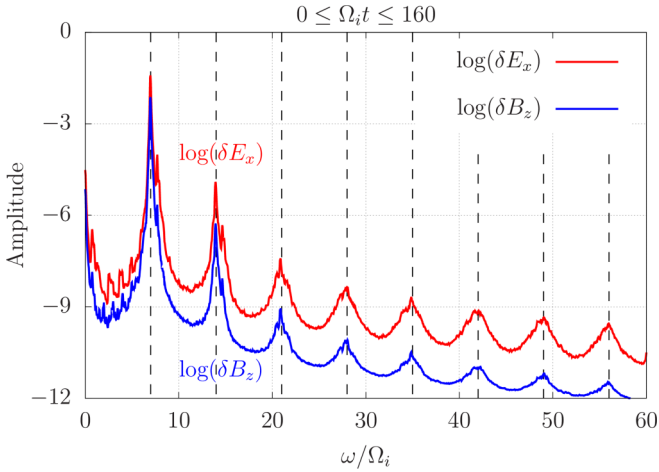


FIG. 3. Frequency spectra of the electric and magnetic field fluctuations obtained from the data for the period of $0 \leq \Omega_i t \leq 160$. The horizontal axis is normalized by Ω_i . The Fourier components, E_x and B_z , are normalized by the background magnetic field (CGS units are used in this paper, unless otherwise noted). The dashed lines indicate integer multiples of $\omega_1 (= 7.0\Omega_i)$. The base of “log” throughout this paper is the natural logarithm.

plasma in this simulation. Because of this, the gradient of the velocity distribution becomes large at $\Omega_i t \simeq 120$. Therefore, the LHWs can be excited by the energetic ions after $\Omega_i t \simeq 80$ and maintain a large amplitude even after $\Omega_i t \simeq 80$.

Finally, we mention the second peak of the perpendicular velocity distribution for $v_\perp/u_\perp \simeq 1.5$ at $\Omega_i t \simeq 120$ and the third but weak peak for $v_\perp/u_\perp \simeq 1.9$ at $\Omega_i t \simeq 160$. Such peaks are observed in the final stage of the simulation and are probably formed by the stochastic acceleration of the energetic ions by the large amplitude LHW [38,39]. A detailed discussion is given in Appendix A. The acceleration of the energetic ions is also confirmed in Fig. 1 where the energy of the energetic ions gradually increases after $\Omega_i t \simeq 80$. The second peak of the velocity distribution cannot contribute to the instabilities [40].

B. Harmonic structure of the LHWs

In this subsection, we investigate the harmonic structure of the LHWs excited by energetic ions. Figure 3 shows the frequency spectra of the electric and magnetic field fluctuations obtained from the data for the period of $0 \leq \Omega_i t \leq 160$. One can see that there are clear peaks at the multiples of $\omega_1 (\simeq 7.0\Omega_i)$, which is slightly smaller than $\omega_{\text{LH}} (\simeq 7.7\Omega_i)$, both in the electric and magnetic field fluctuations. The strongest peak at $\omega_1 = 7.0\Omega_i$ is the LHWs directly excited by energetic ions and the other peaks at $n\omega_1$ are the harmonic LHWs. One can find peaks up to $8\omega_1$. Also, we confirm that peaks are observed up to $11\omega_1$ ($\omega \simeq 10\omega_{\text{LH}}$) in the simulation although their amplitudes are very small (see Appendix B). As expected from Sec. II, the excited LHWs are almost electrostatic because the amplitudes of the electric field fluctuations are significantly larger than those of the magnetic field fluctuations. As the order of the harmonic mode increases, the difference between the amplitudes of the electric and magnetic fields increases. This indicates that the harmonic LHWs with the higher frequency are more electrostatic.

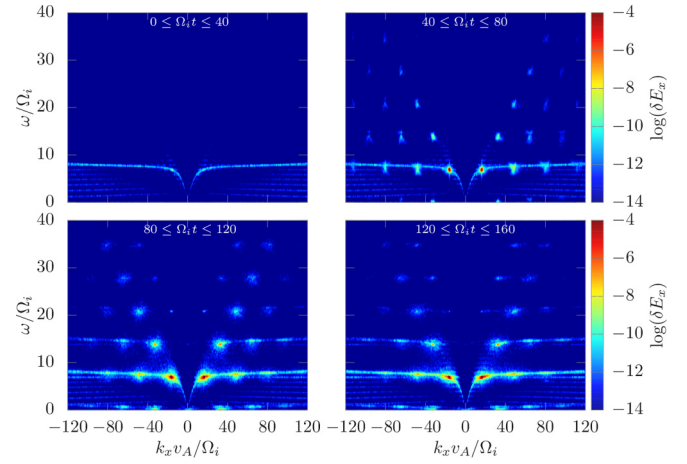


FIG. 4. Wave-number-frequency spectrogram of the electric field fluctuations. The horizontal axis is normalized by Ω_i/v_A .

Next, we investigate the harmonic structure of the LHWs in more detail. Figure 4 shows the wave-number-frequency spectra of the electric field fluctuations for the four periods, $0 \leq \Omega_i t \leq 40$, $40 \leq \Omega_i t \leq 80$, $80 \leq \Omega_i t \leq 120$, and $120 \leq \Omega_i t \leq 160$. The spectra for both positive and negative wave numbers of waves are plotted. Since the instabilities are very weak in the first-quarter period ($0 \leq \Omega_i t \leq 40$), as shown in Fig. 1, the amplitudes of the LHWs are very small in this period. For $40 \leq \Omega_i t \leq 80$, one can find the strongest waves at $(k_x, \omega) \simeq (\pm 16\Omega_i/v_A, 7.0\Omega_i)$, and we define these wave numbers and this frequency as $(k_{\pm 1}, \omega_1)$. Moreover, one can find the many strong waves at multiples of $(k_{\pm 1}, \omega_1)$. This harmonic structure appears as a lattice in the (k_x, ω) plane.

We show that the modes $(k_{\pm 1}, \omega_1)$ are directly excited by the energetic ions but the other waves are not directly excited by them. We can roughly estimate the most unstable wave number k_u of the LHWs as [25]

$$k_u \frac{v_A}{\Omega_i} = \pm \xi_n \frac{v_A}{u_\perp} \frac{u_\perp}{V_{\text{gm}}}. \quad (7)$$

Here, V_{gm} is the speed where the gradient of the perpendicular velocity distribution of the energetic ions is maximum, and ξ_n is given by the condition where the Bessel function $J_n(\xi_n)^2$ is maximum. When $n = 7$, $J_n(\xi_n)^2$ is maximum for $\xi_n \simeq \pm 8.6$ [41]. Setting $u_\perp/v_A = 0.6$ and $V_{\text{gm}}/u_\perp = 0.98$, which is the value at $\Omega_i t = 60$ in Fig. 2, the most unstable wave number for the frequency $\omega = 7\Omega_i$ is $k_u v_A / \Omega_i \sim \pm 14.5$. This is in good agreement with the excited waves (k_1, ω_1) , which indicates that they are directly excited by the ringlike energetic ions. However, the excitation of the other waves such as (k_2, ω_2) and (k_2, ω_0) cannot be explained by this theory. Therefore, these waves are not excited directly by the energetic ions, and can be excited by nonlinear wave-wave coupling.

Here, we consider the modes with the following wave number and frequency:

$$(k_m, \omega_n) = (mk_1, n\omega_1), \quad \begin{cases} m = \pm 1, \pm 2, \dots, \\ n = 0, 1, 2, \dots \end{cases} \quad (8)$$

We refer to the mode $(k_{\pm 1}, \omega_1)$ as the original one, and to the others as harmonic modes. For example, for ω_2 , there are six

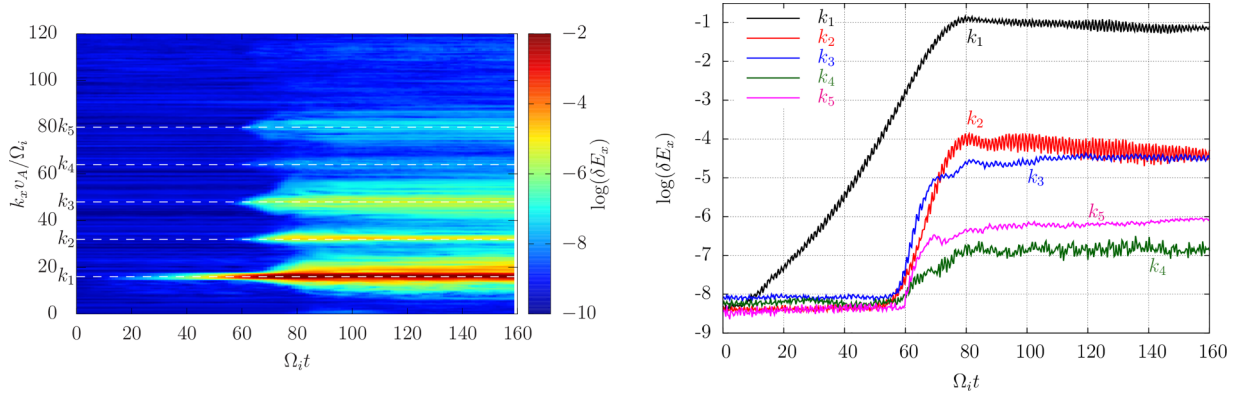


FIG. 5. (Left panel) Time development of $E_x(k_x, t)$. (Right panel) Detailed development of five harmonic modes.

harmonic modes with the wave numbers $k_{\pm 2}$, $k_{\pm 4}$, and $k_{\pm 6}$ in Fig. 4.

We investigate the development of the original and harmonic modes for $80 \leq \Omega_i t \leq 160$, which is the latter half of the simulation. One can find that some harmonic modes disappear and newly appear in this period. This is confirmed by comparing the right-top panel with the lower ones in Fig. 4. The amplitudes of the harmonic modes in the region of the short wavelength and the high frequency, especially $(k_{\pm 6}, \omega_4)$ and $(k_{\pm 7}, \omega_5)$ for $80 \leq \Omega_i t \leq 160$, become much smaller than those for $40 \leq \Omega_i t \leq 80$. However, other harmonic modes with $(k_{\pm 2}, \omega_4)$, $(k_{\pm 3}, \omega_5)$, and $(k_{\pm 4}, \omega_6)$ are newly observed. One can also find that other LHWs around $(k_{\pm 1}, \omega_1)$ are excited in a wider wave number region. This is caused by a change of the perpendicular velocity distribution of the energetic ions [25] shown in Fig. 2. The broadening of the wave number spectrum is also seen in the harmonic modes, especially for ω_2 . This can be explained by nonlinear wave-wave coupling for the broadband wave-number region. Finally, ion Bernstein waves and energetic-ion cyclotron waves with small amplitudes are seen in Fig. 4, and the relationship between the two waves and the harmonic modes will be discussed later.

Next, we show the detailed time development of the original and harmonic modes in Fig. 5. The left panel shows the time development of the Fourier components $E_x(k, t)$ in the (t, k_x) plane, and the dashed lines correspond to the five wave numbers, k_1 , k_2 , k_3 , k_4 , and k_5 . Note that the k_1 mode includes the original mode (k_1, ω_1) , and the k_2 mode includes the three harmonic modes, (k_2, ω_0) , (k_2, ω_2) , and (k_2, ω_4) , as shown in Fig. 4. After the initial growth, the first mode (k_1) begins to grow before $\Omega_i t \simeq 20$, and then its amplitude becomes largest at $\Omega_i t \simeq 80$, which is in good agreement with the collapse time of the perpendicular velocity distribution of the energetic ions in Fig. 2. After $\Omega_i t \simeq 80$, the first mode (k_1) maintains the large amplitudes due to the energetic-ion injection. Other LHWs are excited in the broadband wave-number region around k_1 after $\Omega_i t \simeq 70$ in the left panel of Fig. 5. This is consistent with the broadband excitation of the LHWs around the original mode (k_1, ω_1) in Fig. 4. The four modes with k_2 , k_3 , k_4 , and k_5 are excited at almost the same time, $\Omega_i t \simeq 60$.

The time development of the five wave-number modes, k_1 , k_2 , k_3 , k_4 , and k_5 is clearly shown by the right panel in

Fig. 5. When the amplitude of the first mode (k_1) exceeds $\log(\delta E_x) = -3$ (normalized by the background magnetic field in CGS units), the other four are excited at almost the same time. However, there are somewhat different developments between the four modes. The k_3 mode, which includes the one on the dispersion branch of the LHWs, (k_3, ω_1) , has slightly larger growth rates than the k_2 mode, which does not include those on the dispersion branch of the LHWs. Moreover, after $\Omega_i t \simeq 80$, the k_3 mode continues to gradually grow until the end of the simulation, whereas the amplitude of the k_2 mode gradually decreases. This is also consistent with the time development of k_5 (includes a mode on the branch of the LHWs) and k_4 (does not include a mode on the branch of the LHWs) modes.

Finally, we mention that there are also the harmonic modes below Ω_i , such as $(k_{\pm 2}, \omega_0)$ and $(k_{\pm 4}, \omega_0)$ in Fig. 4. We have not understood which waves are coupled with these harmonic modes, as there are no perpendicularly propagating waves below Ω_i for these wave numbers. The nonlinear wave-wave coupling for waves below Ω_i will be the subject of future work.

C. Nonlinear wave-wave coupling with the harmonic LHWs

To investigate the relationship between the original and harmonic modes, we perform bicoherence analysis which is widely used to evaluate nonlinear wave-wave coupling. Here, we define the bicoherence index as

$$bc(k_A, k_B) = \frac{|\langle E_x(k_A)E_x(k_B)E_x^*(k_C) \rangle|^2}{\langle |E_x(k_A)E_x(k_B)|^2 \rangle \langle |E_x^*(k_C)|^2 \rangle},$$

$$k_C = k_A + k_B, \quad (9)$$

where $*$ denotes a complex conjugate, and brackets $\langle \rangle$ denote the time average for $10\Omega_i^{-1}$. The bicoherence index is between 0 and 1. A large value of the bicoherence index indicates strong wave-wave coupling between three waves with the wave numbers, k_A , k_B , and k_C , while a small value indicates weak wave-wave coupling between the three waves. The bicoherence index is symmetrical around the line of $k_A = k_B$ in the (k_A, k_B) plane. Figure 6 shows the bicoherence index calculated from $E_x(k_x, t)$ shown in Fig. 5 for $51 \leq \Omega_i t \leq 61$

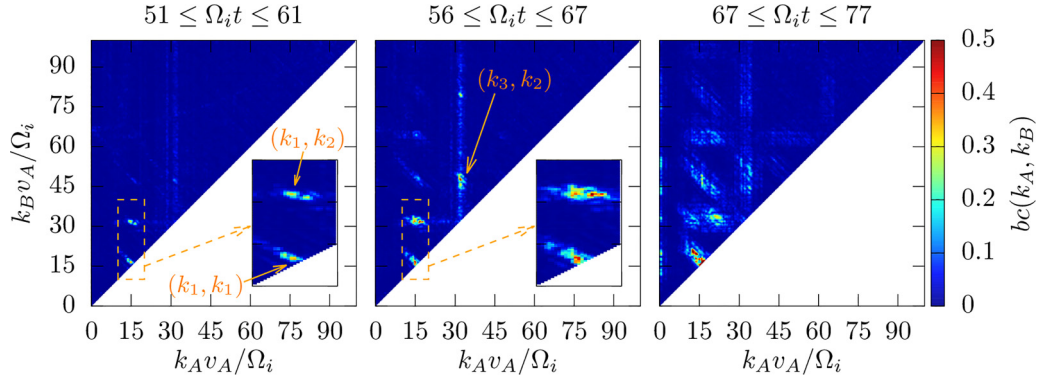


FIG. 6. Bicoherence index calculated by Eq. (9) for three periods. The bicoherence index is between 0 and 1, and is symmetrical around the line of $k_A = k_B$.

(left panel), $56 \leq \Omega_i t \leq 67$ (middle panel), and $67 \leq \Omega_i t \leq 77$ (right panel).

For $51 \leq \Omega_i t \leq 61$, one can find two large bicoherence indices at $(k_A, k_B) \simeq (k_1, k_1)$ and (k_1, k_2) . The large value of the index at (k_1, k_1) indicates the strong wave-wave coupling between the modes with k_1, k_1 , and k_2 . This means that the k_2 mode is excited by coupling between the two k_1 modes. Note that the k_2 mode includes the frequency $\omega \simeq 2\omega_1$. The large value of the index at (k_1, k_2) also indicates that the k_3 mode is excited by the strong wave-wave coupling between the k_1 and k_2 modes. The third harmonic mode also includes the frequency $\omega \simeq 3\omega_1$. Both couplings are consistent with the fact that the two harmonic modes, k_2 and k_3 , begin to grow during this period in Fig. 5.

For $56 \leq \Omega_i t \leq 67$, the previously observed two couplings at $(k_A, k_B) = (k_1, k_1)$ and (k_1, k_2) become stronger. These two stronger couplings are in good agreement with the significant growth of the k_2 and k_3 modes during this period, as shown in the right panel of Fig. 5. Moreover, one can find new strong wave-wave coupling at $(k_A, k_B) = (k_2, k_3)$. This coupling indicates that the k_5 mode is excited by the wave-wave coupling between the k_2 and k_3 modes. However, the wave-wave coupling to excite the k_4 mode [for example, (k_1, k_3) or (k_2, k_2)] is weak, indicating that the k_4 mode cannot grow so much. These results are consistent with the time evolution of each mode during this period shown in Fig. 5.

For $67 \leq \Omega_i t \leq 77$, the amplitude of the k_1 mode is close to the maximum, as shown in the right panel in Fig. 5. During this period one can find the strongest coupling at $(k_A, k_B) \simeq (k_1, k_1)$ and very strong coupling around it in Fig. 6. The coupling in the broadband wave-number region around k_1 can be caused by the broadband excitation of the LHWs around the original mode (k_1, ω_1) , as shown in the left panel of Fig. 4. Also, one can find many other couplings in the broadband wave-number region, such as around (k_1, k_2) and (k_1, k_3) . Finally, some couplings at $k_A \sim 0$ are observed, and this is probably caused by the decay processes of the original or harmonic modes. The detailed coupling processes of the LHWs are discussed in Appendix C.

Thus, we have confirmed that the harmonic modes are excited by nonlinear wave-wave couplings between the original mode driven by the energetic ions and other modes. Note that we have also confirmed the coupling by performing

the bicoherence analysis in frequency, which is described in Appendix D.

D. Which waves are coupled with the harmonic LHWs?

There are no eigenmodes of waves above ω_{LH} in the cold fluid model, but some eigenmodes can exist when thermal or kinetic effects are significant (e.g., see Ref. [42]). To investigate which waves are coupled with the harmonic modes above ω_{LH} , we show two other simulation results.

First, we show the simulation results without energetic ions in the left panel of Fig. 7. In this panel, the LHWs excited by energetic ions and their harmonics are not observed, and the eigenmodes of the LHWs and the ion Bernstein waves (IBWs) are observed. However, when energetic ions exist, energetic-ion cyclotron waves (eICWs) are observed in the right panel of Fig. 7. The eICWs above ω_{LH} are almost electrostatic (see Appendix E). We also confirm that the eICWs are observed up to $\omega \sim 100\Omega_i$, although only up to $\omega \simeq 40\Omega_i$ is shown in this figure. Here, the right panel of Fig. 7 is the same as the left-top panel of Fig. 4 but their color scale is different to clearly show the IBWs/eICWs with small amplitudes. We discuss the relationship between the IBWs/eICWs and the harmonic modes of the LHWs. Comparing the two panels in Fig. 7, one can clearly see that the excitation regions of the eICWs and IBWs are different. The IBWs, due to the bulk ions, have large amplitudes for $\omega \leq \omega_{LH}$ in the short-wavelength region. However, the eICWs, due to the energetic ions, have large amplitudes for $\omega \geq \omega_{LH}$ in the long-wavelength region. The

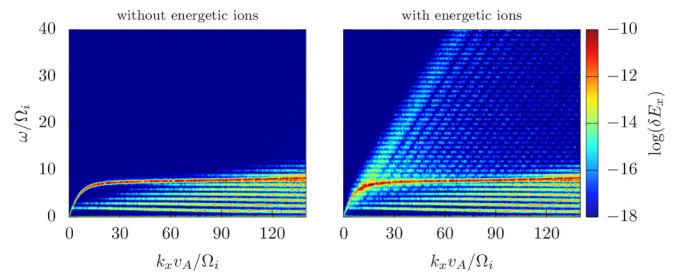


FIG. 7. Wave-number-frequency spectra of the electric field fluctuations during the period of $0 \leq \Omega_i t \leq 40$ for the two cases: without (left panel) and with (right panel) energetic ions. The other simulation parameters are the same for the two cases.

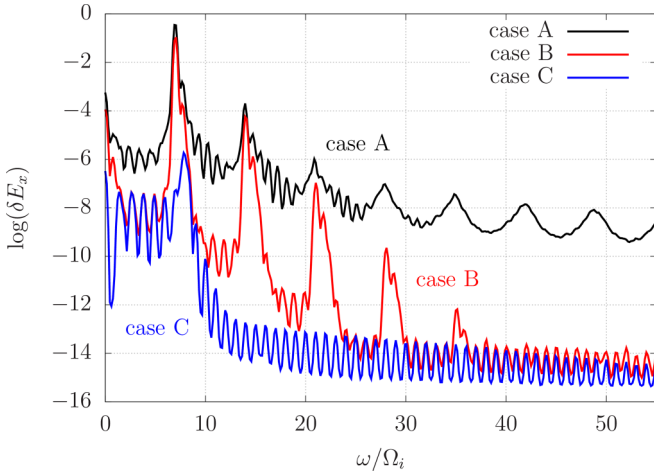


FIG. 8. Frequency spectra of the electric field fluctuations for $80 \leq \Omega_i t \leq 120$ (same format as in Fig. 3). Three cases, where energetic ions are continuously injected after $\Omega_i t = 80$ (case A), removed at $\Omega_i t = 80$ (case B), and do not exist from the beginning (case C), are plotted.

amplitudes of the eICWs decrease as the wave number and the frequency increase. Comparing the right panel in Fig. 7 with the right-top one in Fig. 4, one can find that the excitation region of the harmonic modes, especially with (k_l, ω_l) ($l = 2, 3, \dots$), overlaps with that of the eICWs. In addition, the fact that the amplitudes decrease as the wave number and the frequency increase is consistent between the eICWs and the harmonic modes. Therefore, these results indicate that the harmonic modes with $\omega > \omega_{LH}$ are coupled with the eICWs.

Next, we perform another simulation for the case where the energetic ions (and the same number of electrons) disappear in the middle of the simulation period; at $\Omega_i t \simeq 80$, all the injected energetic ions and electrons are artificially removed. This means that until $\Omega_i t = 80$, the simulation results are exactly the same as those shown in the previous section. We investigate how the loss of the energetic ions affects the development of the harmonic modes after $\Omega_i t \simeq 80$. Figure 8 shows the frequency spectra of the electric field fluctuations for the three cases, where energetic ions are continuously injected after $\Omega_i t = 80$ (case A), removed at $\Omega_i t = 80$ (case B), and do not exist from the beginning (case C). One can easily see that the higher harmonic modes for $n > 5$ in case B are damped due to the loss of the energetic ions. The amplitudes of the harmonic modes for $n = 4$ and 5 in case B are much smaller than those in case A, but change significantly less for $n = 2$ and 3. The strong decay and damping of the harmonic modes with $n \geq 4$ are consistent with the damping of the eICWs, whose amplitudes other than the harmonic modes for $\omega \geq 24\Omega_i$ are almost the same as those in case C. It indicates that higher harmonic modes are coupled with the eICWs.

However, the fact that the lower harmonic modes ($n = 2, 3$) can exist even after the loss of energetic ions indicates that other waves, apart from the eICWs, are coupled with the harmonic modes. To study this, we show the wave-number-frequency spectra of case A in Fig. 9. By comparing Fig. 9 and the left panel of Fig. 7, one can see that the amplitudes of the IBWs for $\omega > \omega_{LH}$ in the short-wavelength region become much larger in case A than those in case C. This is because the

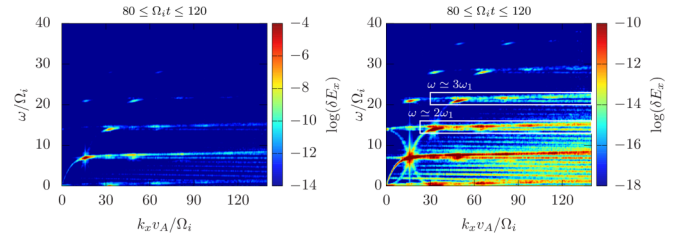


FIG. 9. Wave-number-frequency spectra of the electric field fluctuations for case B (energetic ions are removed at $\Omega_i t \simeq 80$) with two different color scales.

bulk ions driving the IBWs have obtained a large amount of energy from the LHWs by the time of the loss of energetic ions (see Fig. 1). Moreover, the IBWs near $\omega \simeq 2\omega_1$ and $3\omega_1$ in the broadband wave-number region also have large amplitudes, and those of the harmonic modes in this region ($n = 2, 3$) remain large. This indicates that the IBWs near $\omega \simeq 2\omega_1$ and $3\omega_1$ can substitute for the eICWs and be coupled with the lower harmonic modes.

Thus, summarizing the simulation results presented so far, after the original mode is directly excited by the energetic ions, the harmonic modes are excited by the nonlinear wave-wave couplings. The harmonic modes above ω_{LH} can exist without significant damping because they can be on the branch of the eICWs or IBWs. However, when the eICWs are damped due to the disappearance of the energetic ions, the harmonic modes on the branch of the eICWs are damped whereas those on the branch of the IBWs can exist.

IV. DISCUSSION

A. Comparison with the initial value problem

In this subsection, we compare the initial value problem and the injection model to investigate how the energetic-ion injection affects the development of the harmonic modes. Initial value problems, where energetic ions are set at the initial time, are often used to study the excitation process of LHWs. In this problem, after the collapse of the velocity distribution of the energetic ions, the free energy to excite the LHWs is exhausted, and the excited waves are damped.

The density of the energetic ions in the initial value problem is 0.5% of the bulk ions, which is the same as the time-averaged density in the injection model. The other parameters are the same as in the injection model. The upper panel of Fig. 10 shows the energy development of the harmonic modes in the injection model and the initial value problem. The energy of the harmonic modes (H_E) is defined by the following equation:

$$H_E \equiv \int_0^{140\Omega_i/v_A} dk \int_{1.3\omega_{LH}}^{5\omega_{LH}} d\omega E_x^2(k, \omega). \quad (10)$$

The four harmonic modes ($n = 2, 3, 4, 5$) are included in H_E . The Fourier component $E_x(k_x, \omega)$ is obtained for every $20\Omega_i^{-1}$ with the simulation period $0 \leq \Omega_i t \leq 160$. The value of H_E is normalized by the maximum value in the initial value problem.

In the initial value problem, the value of H_E for $40 \leq \Omega_i t \leq 60$ is maximum. After that, H_E rapidly decreases and

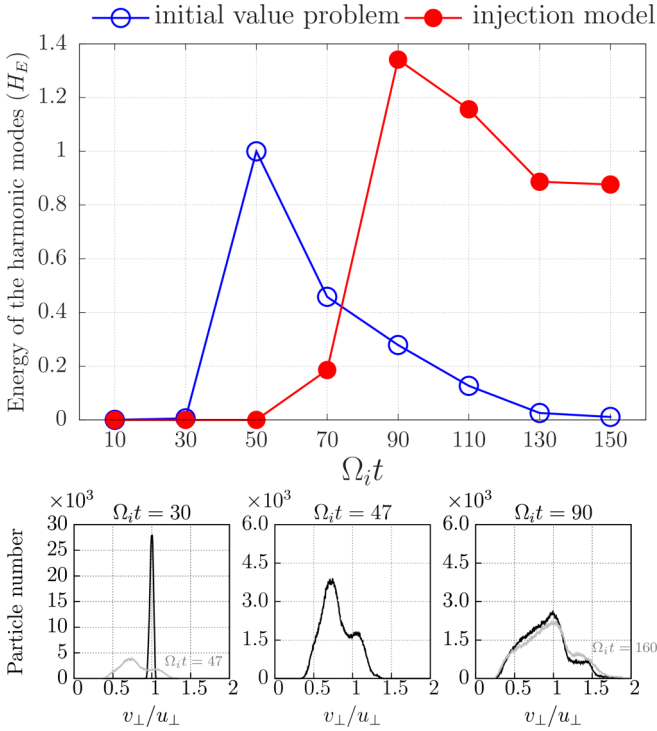


FIG. 10. (Upper panel) Energy development of the harmonic modes within the injection model and the initial value problem. The energy of the harmonic modes (H_E) is defined by Eq. (10). The value of H_E is normalized by the maximum value within the initial value problem. (Lower panels) Snapshots of the velocity distribution of the energetic ions in the initial value problem with the same format as in Fig. 2. The time $\Omega_i t \simeq 47$ corresponds to the collapse time of the energetic-ion velocity distribution.

finally becomes about 1% of the maximum value. The snapshots of the velocity distribution in the lower panels of Fig. 10 show that the ability to excite the original modes is significantly reduced after the collapse time at $\Omega_i t \simeq 47$, which leads to damping of the original modes.

This strong decay of the harmonic modes is due to the damping of the original modes because the harmonic ones are supported by the original ones driven by the energetic ions, as shown in Sec. III.

However, the energy of the harmonic modes (H_E) remains very large in the injection model. The value of H_E after the peak time is more than 80% of the maximum H_E in the initial value problem. In the injection model, the original modes also maintain large amplitudes due to the newly injected energetic ions, such that the harmonic modes maintain large amplitudes even after the peak time. Additionally, the maximum value of H_E is about 1.3 times larger than that in the initial value problem.

Thus, we have confirmed that energetic-ion injection plays a crucial role in sustaining the large amplitudes of the harmonic modes.

B. Dependence of frequency ratio ω_{pe}/Ω_e

In this subsection, we investigate the development of the harmonic modes in the case of the frequency ratio ω_{pe}/Ω_e

being higher. The higher frequency ratio, ω_{pe}/Ω_e , means higher density or weaker magnetic field conditions. To focus on the dependence of the frequency ratio, the following parameters are set to the same values as for the simulation in Sec. III: electron thermal velocity, the ratio of the ring velocity to the Alfvén velocity, and the density ratio of energetic ions to bulk ions.

Figure 11 shows the simulation results for $\omega_{pe}/\Omega_e = 0.5$ and 0.75 . For these simulation parameters, the lower hybrid resonance frequencies are $\omega_{LH} \simeq 14.2\Omega_i, 19.0\Omega_i$, respectively, and the ratio $|E_x/B_z|$ given by Eq. (6) is smaller than that for $\omega_{pe}/\Omega_e = 0.25$. The left panels show the frequency spectra for $\omega_{pe}/\Omega_e = 0.5$ and 0.75 in the same format as in Fig. 3. Comparing the amplitudes of the harmonic modes with the same order (for example, $n = 2$) for $\omega_{pe}/\Omega_e = 0.25$ (see Fig. 3), they are clearly smaller as ω_{pe}/Ω_e increases. Furthermore, for $\omega_{pe}/\Omega_e = 0.75$, the amplitudes of the harmonic modes for $n \geq 3$ are negligibly small. This is also confirmed by the wave-number-frequency spectra in the right panels of Fig. 11. The clear lattice pattern in the (k_x, ω) plane is not observed for $\omega_{pe}/\Omega_e = 0.5$ and 0.75 . However, for $\omega_{pe}/\Omega_e = 0.5$, the LHWs around ω_{LH} are excited in the broadband wave-number region. These waves are directly excited by the energetic ions, and the broadening of the wave-number region is due to the change of the velocity distribution of the energetic ions. Associated with this, the harmonic modes for $\omega \simeq 2\omega_{LH}$ are excited in the broadband wave-number region. Thus, these results indicate that the higher harmonic modes are unlikely to be excited under the condition with relatively higher ω_{pe}/Ω_e .

C. Comparison with experimental observations

Based on the simulation results, we now discuss the conditions under which harmonic LHWs in Earth's magnetosphere are excited and observed even though energetic ions were not observed. The plasma parameters used in our simulations are different from the parameters when the harmonic LHWs were observed. However, considering that such comparisons have never been done, this attempt gives insight into the excitation and development of the harmonic LHWs in Earth's magnetosphere.

First, as illustrated in Fig. 8, we have shown that the harmonic LHWs with a lower order (up to third order) can exist even after energetic ions disappear. The existence of the harmonic LHWs is supported by the coupling with IBWs, which have large amplitudes because bulk ions are accelerated by the LHWs. This result helps explain the observation, where energetic ions, which are believed to excite the LHWs, have not been found. In other words, the harmonic LHWs might be observed after the energetic ions exciting the LHWs have disappeared.

Second, from the observations, the harmonic LHWs are observed for at least 1.5 s with a background magnetic field of 20 nT. However, for the initial value problem in Fig. 10, the energy of the harmonic modes after the peak time decreases to $1/e$ at $\Omega_i t \simeq 40$. Assuming that the background magnetic field is 20 nT and the mass ratio is $m_i/m_e = 1000$, this decay time corresponds to $\Delta t \simeq 11.4$ s, which is larger than the observed decay time. The harmonic LHWs can be interpreted as being

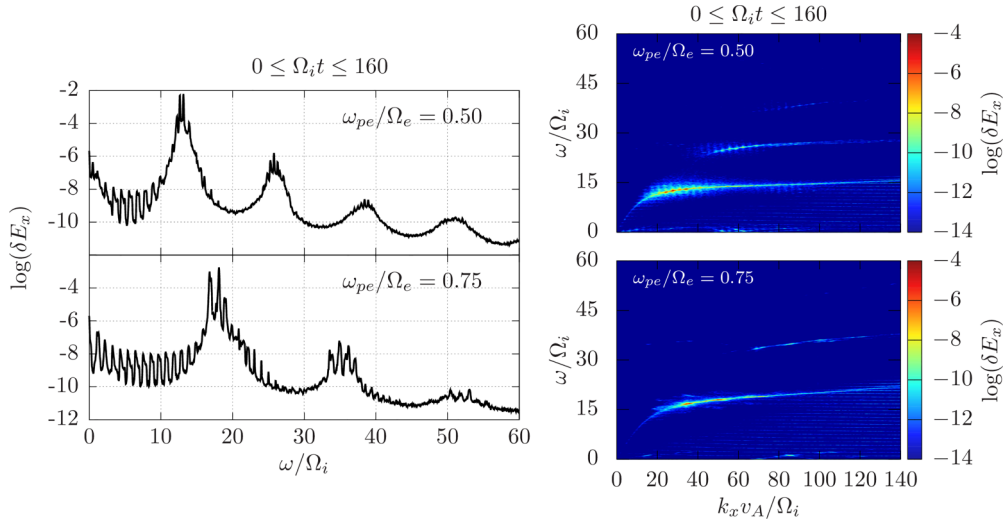


FIG. 11. (Left panel) Frequency spectra of the electric field fluctuations for $\omega_{pe}/\Omega_e = 0.5$ and 0.75 obtained by integrating $E_x(k_x, \omega)$ over the wave-number range $0 \leq k_x v_A/\Omega_i \leq 140$. (Right panels) Wave-number-frequency spectra of the electric field fluctuations for $\omega_{pe}/\Omega_e = 0.5$ and 0.75 (same format as in Fig. 4).

observed by the spacecraft after the velocity distribution of the energetic ions has collapsed but before these waves decay. The energetic ions were not injected for a long time but were likely injected instantaneously. This interpretation is consistent with the fact that the energetic ions were not found in the observation.

Third, as illustrated in Fig. 11, we have shown that the harmonic LHWs are likely to be excited under conditions where the LHWs directly excited by energetic ions have dominantly electrostatic components. The frequency ratio (ω_{pe}/Ω_e) has to be lower to excite more electrostatic LHWs, as predicted by Eq. (6). The same is true for the velocity ratio (u_{\perp}/v_A). This result indicates that the observed harmonic LHWs might be excited by energetic ions with a smaller ring velocity than the Alfvén velocity under low ω_{pe}/Ω_e conditions (equivalent to relatively strong magnetic field or small density conditions).

V. SUMMARY

In this paper, we performed one-dimensional, electromagnetic, particle-in-cell simulations to study the harmonic structure of the LHWs driven by energetic ions at low ω_{pe}/Ω_e . To investigate the long-term development of the harmonic LHWs, the effects of energetic ion injection are considered in the simulations. We have shown that the harmonic LHWs are generated at many wave numbers and frequencies by nonlinear wave-wave coupling. The frequency of the harmonic LHWs extends up to ten times ω_{LH} .

We have shown that the energetic ions excite the LHWs first, and then the harmonic LHWs begin to be excited at almost the same time. The harmonic LHWs have integer multiples of the frequency and the wave number of the original LHWs directly excited by the energetic ions. Bicoherence analysis indicates that the harmonic LHWs are excited by nonlinear wave-wave coupling. To investigate which waves are coupled with the harmonic LHWs, we also perform other simulations for the case where energetic ions are artificially

removed in the middle of the simulation period. These additional simulation results have shown that the harmonic LHWs are coupled with the ion cyclotron waves due to energetic ions and that ion Bernstein waves can also be coupled with the harmonic LHWs if the energetic ions disappear. It could also be mentioned that the magnetospheric observations may be consistent with the energetic ion generation mechanism of the LHWs based on the simulations.

The effects of energetic ion injection and the dependence of the frequency ratio, ω_{pe}/Ω_e , on the development of the harmonic LHWs are investigated. We have shown that energetic ion injection plays a crucial role in sustaining the large amplitudes of the harmonic LHWs. At higher frequency ratios (equivalent to relatively weak magnetic field or large density conditions), the harmonic LHWs are unlikely to be excited, especially in the high-frequency region.

In this paper, we performed one-dimensional particle-in-cell simulations where the waves propagating perpendicular to the magnetic field are considered. It is unclear how the harmonic LHWs interact with other waves propagating in various directions. Therefore, in the near future, we will perform two-dimensional particle-in-cell simulations, including effects of such waves, to investigate the excitation and development of the harmonic LHWs.

ACKNOWLEDGMENTS

This work was performed on the “Plasma Simulator” (NEC SX-Aurora TSUBASA) of NIFS with the support and under the auspices of the NIFS Collaboration Research program (Grants No. NIFS21KNSS164, No. NIFS22KISS008, and No. NIFS22KISS016). This work was supported by JST SPRING, Grant No. JPMJSP2110, and JSPS KAKENHI Grants No. 22J15207, No. 22K03570, and No. 22KJ1887. This work is supported by the “Joint Usage/Research Center for Interdisciplinary Large-scale Information Infrastructures” and the “High Performance Computing Infrastructure” in

Japan (Projects No JH210005-NAH and No. JH220004-NAH). Finally, we thank the two anonymous referees for their constructive comments.

APPENDIX A: STOCHASTIC ACCELERATION BY THE LHWs

Many studies showed that ion motion becomes stochastic in a large amplitude electrostatic wave propagating perpendicular to the magnetic field (e.g., Refs. [38,39]). Particularly, Ref. [38] predicts that peaks of the ion velocity distribution can form by stochastic acceleration due to a large amplitude LHW. We find that the second peak of the energetic-ion velocity distribution shown in Fig. 2 can be explained by the stochastic acceleration driven by the dominant large amplitude LHW. The peak velocity determined by the separatrix velocity agrees well with the theory in Ref. [38].

Here, for simplicity, we assume that only the dominant LHW contributes to the stochastic acceleration. The separatrix, which determines the trapped region of ions, can be given by the zero points of the Bessel function, $J_n(k_x v_\perp / \Omega_i) = 0$. When $n = 7$ ($\omega_{LH} \simeq 7.0\Omega_i$), the zero points of the Bessel function, $J_7(k_x v_\perp / \Omega_i)$, are

$$k_x v_\perp / \Omega_i = 0, 11.08, 14.82, \dots \quad (\text{A1})$$

Using the parameter ($u_\perp / v_A = 0.6$) and the dominant wave number of the LHW ($k_x v_A / \Omega_i = 16$), the separatrix velocity of the energetic ions (v_\perp / u_\perp) can be obtained as

$$\frac{v_\perp}{u_\perp} \simeq 0, 1.15, 1.54, 1.90, \dots \quad (\text{A2})$$

This means that there are trapped regions for $0 \leq v_\perp / u_\perp \leq 1.15$, $1.15 \leq v_\perp / u_\perp \leq 1.54$, and $1.54 \leq v_\perp / u_\perp \leq 1.90, \dots$, and ions in a trapped region cannot move to another region. However, if the wave amplitude is large, then ions are stochastically accelerated and they can move to another region. These separatrix velocities agree well with the peak velocity of the energetic-ion distribution in Fig. 2. The velocity distribution of energetic ions at $\Omega_i t \simeq 80$ significantly decreases for $v_\perp / u_\perp \geq 1.15$, indicating that fewer energetic ions can move to the adjacent region, $1.15 \leq v_\perp / u_\perp \leq 1.54$. At $\Omega_i t \simeq 120$, although many energetic ions are in the region, $1.15 \leq v_\perp / u_\perp \leq 1.54$, very few energetic ions can cross the separatrix velocity, $v_\perp / u_\perp \simeq 1.54$, and they remain around there. As a result, the second peak can form. Finally, Eq. (A2) also predicts the third peak at $v_\perp / u_\perp \simeq 1.9$. The weak third peak can be seen at $v_\perp / u_\perp \simeq 1.9$ at the end of the simulation $\Omega_i t \simeq 160$ in Fig. 2.

APPENDIX B: HIGH-FREQUENCY HARMONIC LHWs

The lattice pattern of the harmonic structure of the LHWs shown in Fig. 4 is clearly seen in Fig. 12. One can see that many harmonic modes are excited in the broadband wave-number and frequency regions. The maximum orders of the harmonic modes exceed $m = 10$ and $n = 10$, respectively. Particularly, the maximum frequency ($\omega \simeq 11\omega_1 \simeq 10\omega_{LH}$) observed in this simulation is much higher than the frequency of unusual waves above ω_{LH} , reported so far in the simulations and observations [23–25,31].

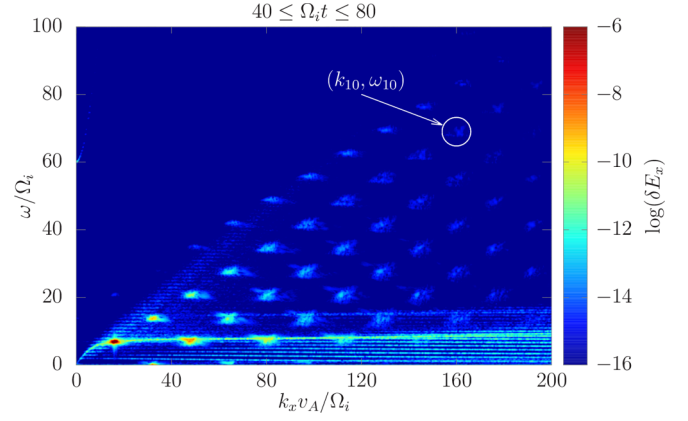


FIG. 12. Wave-number-frequency spectrum of the electric field fluctuations (similar to the right-top panel of Fig. 4, but with a different color scale).

APPENDIX C: COUPLING PROCESS OF THE HARMONIC LHWs

In general, the wave-wave coupling processes can be divided into two types: coalescence and decay. In the coalescence process, one wave merges with another to excite a third, expressed as $(\mathbf{k}_A, \omega_A) + (\mathbf{k}_B, \omega_B) = (\mathbf{k}_C, \omega_C)$ for $\omega_A, \omega_B, \omega_C > 0$. Figure 13 illustrates the coalescence and decay processes in the simulation shown in the main text. For example, the original mode with (k_1, ω_1) merges with itself to excite the harmonic mode (k_2, ω_2) , and merges with the harmonic mode (k_3, ω_3) to excite the harmonic mode (k_4, ω_4) . By considering the original and harmonic LHWs propagating in the opposite direction, the higher harmonic modes such as (k_2, ω_4) , observed in the latter half of the simulation (see Fig. 4), can be explained by merging the original mode $(-k_1, \omega_1)$ with the harmonic mode (k_3, ω_3) . Thus, the coalescence process results in wave-wave coupling such that the frequency of the excited waves increases.

However, in the decay process, one wave decays into two, expressed as $(\mathbf{k}_A, \omega_A) = (\mathbf{k}_B, \omega_B) + (\mathbf{k}_C, \omega_C)$ for $\omega_A, \omega_B, \omega_C > 0$. For example, the original mode (k_1, ω_1) decays into the original mode $(-k_1, \omega_1)$ and the harmonic mode (k_2, ω_2) , and the harmonic mode (k_3, ω_3) decays into the original mode (k_1, ω_1) and the harmonic mode (k_4, ω_4) . Thus,

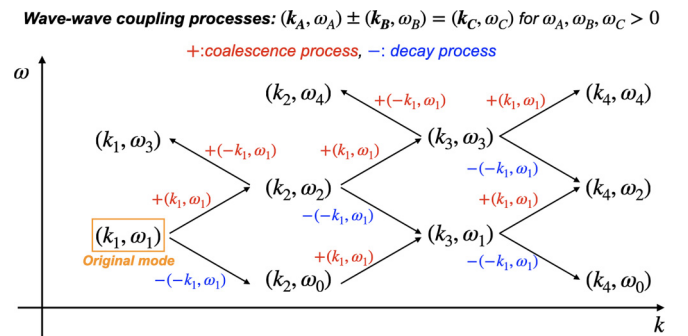


FIG. 13. Illustration of coupling processes leading to the harmonic structure of the LHWs.

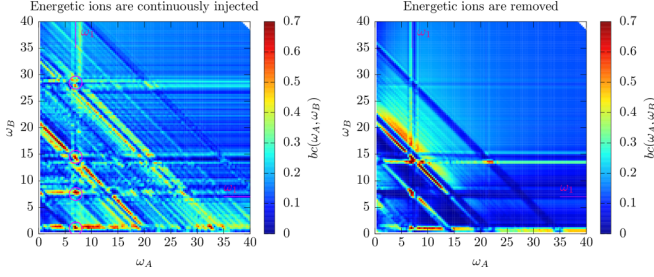


FIG. 14. Bicoherence index in frequency calculated by Eq. (D1) for the two cases where energetic ions are continuously injected (left panel) as shown in Fig. 4 and removed (right panel) as shown in Fig. 9. The frequencies ω_A , ω_B , and ω_C are normalized by Ω_i .

the decay process results in wave-wave coupling such that the frequency of the excited waves decreases.

In addition to the processes stated above, there are many other coalescence and decay ones, and the harmonic modes can be excited by them.

APPENDIX D: BICOHERENCE ANALYSIS IN FREQUENCY

In this Appendix, we show nonlinear wave-wave coupling between the original and harmonic modes by performing the bicoherence analysis in frequency. The bicoherence index in frequency is defined as

$$bc(\omega_A, \omega_B) = \frac{|\langle E_{x,k_1}(\omega_A)E_{x,k_2}(\omega_B)E_{x,k_3}^*(\omega_C) \rangle|^2}{\langle |E_{x,k_1}(\omega_A)E_{x,k_2}(\omega_B)|^2 \rangle \langle |E_{x,k_3}^*(\omega_C)|^2 \rangle},$$

$$\omega_C = \omega_A + \omega_B. \quad (\text{D1})$$

Here, to calculate the bicoherence index in frequency, we divide the simulation period into eight periods of $\Omega_i \Delta t \simeq 20$. We then obtain the frequency spectra, $E_{x,k_1}(\omega)$, $E_{x,k_2}(\omega)$, and $E_{x,k_3}(\omega)$, with the wave numbers, $k_1 v_A / \Omega_i \simeq 16$, $k_2 = 2k_1$, and $k_3 = 3k_1$, in the eight periods, respectively. By taking the time average of the eight periods, we calculate the bicoherence index in frequency. From Fig. 4, we see that the frequency spectrum $E_{x,k_1}(\omega)$ includes the original mode (k_1, ω_1) and the harmonic mode (k_1, ω_3) ; $E_{x,k_2}(\omega)$ includes the harmonic modes (k_2, ω_0) , (k_2, ω_2) , (k_2, ω_4) ; $E_{x,k_3}(\omega)$ includes the harmonic modes (k_3, ω_1) , (k_3, ω_3) , and (k_3, ω_5) .

Figure 14 shows the bicoherence index for the two cases where energetic ions are continuously injected (left panel) as shown in Fig. 4 and removed (right panel) as shown in Fig. 9. Different from $bc(k_A, k_B)$, the bicoherence index, $bc(\omega_A, \omega_B)$, is not symmetrical around the line $\omega_A = \omega_B$ because three different electric fields are used to calculate $bc(\omega_A, \omega_B)$.

In the left panel, one can see the large values of $bc(\omega_A, \omega_B)$ for $\omega_A \simeq 7.0 = \omega_1$, which are marked by magenta solid circles. This means strong wave-wave couplings at the four points: $(\omega_A, \omega_B, \omega_C) = (\omega_1, \omega_0 \sim 0, \omega_1 + \omega_0)$, $(\omega_1, \omega_1, \omega_2)$, $(\omega_1, \omega_2, \omega_3)$, and $(\omega_1, \omega_4, \omega_5)$. Taking into account the wave numbers of $E_{x,k_1}(\omega_A)$, $E_{x,k_2}(\omega_B)$, and $E_{x,k_3}(\omega_C)$, the large index, for example, at $(\omega_A, \omega_B) = (\omega_1, \omega_2)$ indicates that the original mode (k_1, ω_1) of E_{x,k_1} is strongly coupled with the harmonic mode (k_2, ω_2) of E_{x,k_2} to excite the harmonic mode

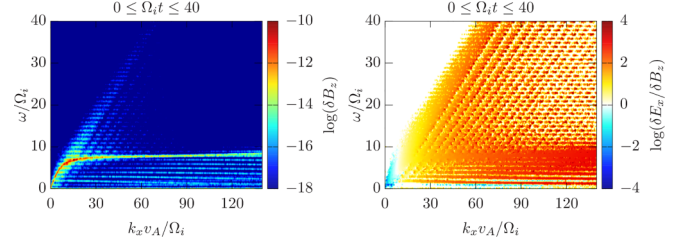


FIG. 15. Wave-number-frequency spectra of the magnetic field fluctuation amplitudes (left panel) and the ratio of the electric to magnetic field fluctuations (right panel). In the right panel, the white color indicates that no waves except those on the branch of the LHWs exist.

(k_3, ω_3) of E_{x,k_3} . The other harmonic modes of $E_{x,k_3}(\omega_C)$ can be similarly excited by coupling between $E_{x,k_1}(\omega_A)$ and $E_{x,k_2}(\omega_B)$. Thus, we have also confirmed that nonlinear wave-wave couplings excite the harmonic LHWs by performing the bicoherence analysis in frequency.

Moderate coupling can be seen for $\omega_B \leq \omega_1$ on the line $\omega_A + \omega_B - n\Omega_i \simeq 0$. This periodic coupling indicates nonlinear wave-wave coupling between the eICWs/IBWs of E_{x,k_1} and the IBWs of E_{x,k_2} . However, for $\omega_B \geq \omega_1$, other moderate couplings can be seen on the lines $\omega_A + \omega_B \simeq 20\Omega_i$ and $\omega_A + \omega_B \simeq 35\Omega_i$. They might be between the eICWs and IBWs, but we do not give further discussion due to the reasons described below.

In the right panel, paying attention to the region for $\omega_B \leq \omega_1$ one can see that the coupling is clearly suppressed. The small $bc(\omega_A, \omega_B)$ in the region of $\omega_B \leq \omega_1$ means that the eICWs no longer take part in the coupling, which is consistent with the result in Fig. 9 where the eICWs are damped due to loss of the energetic ions. However, strong coupling can be seen for $\omega_A = \omega_1$ and at $(\omega_A, \omega_B) = (\omega_3, \omega_2)$. Considering the fact that the higher harmonic modes decrease in amplitudes as shown in Fig. 8, these strong couplings can be interpreted as the decay process of the higher harmonic modes. There is some periodic coupling above the line $\omega_A + \omega_B \simeq 20\Omega_i$. This might be the coupling between the IBWs, but we do not give further discussion.

The bicoherence analysis in frequency can give further insights into nonlinear wave-wave couplings, but the following problems should be noted when interpreting the results. The bicoherence analysis in wave number can be easily calculated with a high resolution in time average when using the wave-number spectra $E(k, t)$, but one in frequency cannot be easily calculated when using the frequency spectra $E(\omega, t)$ (It takes more computational cost to perform an ensemble average of the frequency spectra instead of a time average). Since the bicoherence index in frequency is calculated based on the frequency spectra $E_x(\omega)$ in the eight periods, the time average can be somewhat rough. Therefore, there may be some unphysical noise included in the bicoherence index in frequency. Second, the bicoherence index only indicates the strength of nonlinear wave-wave coupling between three waves. In other words, a larger index does not necessarily mean that the amplitude of the waves actually excited is larger.

Although the bicoherence analysis in frequency gives a lot of information about nonlinear wave-wave coupling, the

identification can be difficult and requires a high-cost analysis, which is beyond the scope of our study.

APPENDIX E: CHARACTERISTICS OF EICWS

Figure 15 shows the wave-number-frequency spectra of the magnetic field fluctuations (left panel) and the ratio of the

electric to magnetic field fluctuations (right panel) in the same format as Fig. 9. One can see that the amplitudes of the eICWs and the value of $\log(\delta E_x/\delta B_z)$ decrease as the wave number and the frequency increase. The latter means that the eICWs are almost electrostatic in the region of high frequency and short wavelength.

-
- [1] A. L. Verdon, I. H. Cairns, D. B. Melrose, and P. A. Robinson, *Phys. Plasmas* **16**, 052105 (2009).
- [2] V. D. Shapiro, V. I. Shevchenko, A. S. Sharma, K. Papadopoulos, R. Z. Sadgeev, and V. B. Lebedev, *J. Geophys. Res.: Space Phys.* **98**, 1325 (1993).
- [3] K. Saito, H. Igami, M. Toida, T. Akiyama, S. Kamio, R. Seki, and L. E. Group, *Plasma Fusion Res.* **13**, 3402043 (2018).
- [4] S. G. Thatipamula, M. H. Kim, J. Kim, J. H. Kim, and G. S. Yun, *Plasma Phys. Controlled Fusion* **62**, 035004 (2020).
- [5] X. Liu, L. Chen, and Q. Ma, *Geophys. Res. Lett.* **48**, e2021GL093168 (2021).
- [6] M. André, P. Norqvist, L. Andersson, L. Eliasson, A. I. Eriksson, L. Blomberg, R. E. Erlandson, and J. Waldemark, *J. Geophys. Res.: Space Phys.* **103**, 4199 (1998).
- [7] Z. Yuan, X. Yu, S. Huang, Z. Qiao, F. Yao, and H. O. Funsten, *J. Geophys. Res.: Space Phys.* **123**, 1242 (2018).
- [8] S. Hill, N. Buzulukova, S. Boardsen, and M.-C. Fok, *J. Geophys. Res.: Space Phys.* **125**, e2019JA027210 (2020).
- [9] R. B. Horne, R. M. Thorne, S. A. Glauert, N. P. Meredith, D. Pokhotelov, and O. Santolk, *Geophys. Res. Lett.* **34**, L17107 (2007).
- [10] F. Xiao, Q. Zong, Y. Wang, Z. He, Z. Su, C. Yang, and Q. Zhou, *Sci. Rep.* **4**, 5190 (2014).
- [11] B. Eliasson and K. Papadopoulos, *J. Geophys. Res.: Space Phys.* **113**, A09315 (2008).
- [12] E. V. Mishin, M. J. Starks, G. P. Ginet, and R. A. Quinn, *Geophys. Res. Lett.* **37**, L04101 (2010).
- [13] E. Camporeale, G. L. Delzanno, and P. Colestock, *J. Geophys. Res.: Space Phys.* **117**, A10315 (2012).
- [14] X. Shao, B. Eliasson, A. S. Sharma, G. Milikh, and K. Papadopoulos, *J. Geophys. Res.: Space Phys.* **117** (2012).
- [15] X. Xu, L. Chen, C. Zhou, X. Liu, Z. Xia, J. J. Simpson, and Y. Zhang, *J. Geophys. Res.: Space Phys.* **125**, e2019JA027750 (2020).
- [16] K. Akimoto, K. Papadopoulos, and D. Winske, *J. Plasma Phys.* **34**, 445 (1985).
- [17] N. P. Meredith, R. B. Horne, and R. R. Anderson, *J. Geophys. Res.* **113**, A06213 (2008).
- [18] Q. Ma, W. Li, L. Chen, R. M. Thorne, and V. Angelopoulos, *J. Geophys. Res.: Space Phys.* **119**, 844 (2014).
- [19] D. Winske and W. Daughton, *Phys. Plasmas* **19**, 072109 (2012).
- [20] D. Winske and W. Daughton, *Phys. Plasmas* **22**, 022102 (2015).
- [21] M. Toida, K. Saito, H. Igami, T. Akiyama, S. Kamio, and R. Seki, *Plasma Fusion Res.* **13**, 3403015 (2018).
- [22] Z. Yuan, Z. Ouyang, X. Yu, S. Huang, F. Yao, and H. O. Funsten, *Geophys. Res. Lett.* **45**, 10,160 (2018).
- [23] B. Chapman, R. O. Dendy, S. C. Chapman, K. G. McClements, G. S. Yun, S. G. Thatipamula, and M. Kim, *Nucl. Fusion* **58**, 096027 (2018).
- [24] K. Min and K. Liu, *J. Geophys. Res.: Space Phys.* **120**, 2739 (2015).
- [25] T. Kotani, M. Toida, T. Moritaka, and S. Taguchi, *J. Phys. Soc. Jpn.* **90**, 124501 (2021).
- [26] F. S. McDermott, G. Bekefi, K. E. Hackett, J. S. Levine, and M. Porkolab, *Phys. Fluids* **25**, 1488 (1982).
- [27] S. K. Hansen, S. K. Nielsen, M. Salewski, M. Stejner, J. Stober, and the ASDEX Upgrade team, *Plasma Phys. Controlled Fusion* **59**, 105006 (2017).
- [28] S. K. Hansen, S. K. Nielsen, J. Stober, J. Rasmussen, M. Salewski, M. Stejner, and A. U. Team, *Phys. Plasmas* **26**, 062102 (2019).
- [29] M. G. Senstius, S. K. Nielsen, R. G. Vann, and S. K. Hansen, *Plasma Phys. Controlled Fusion* **62**, 025010 (2019).
- [30] J. Han, Z. Gao, and S. K. Hansen, *Phys. Plasmas* **30**, 022104 (2023).
- [31] S. Y. Huang, D. Deng, Z. G. Yuan, K. Jiang, J. X. Li, X. H. Deng, X. D. Yu, L. H. He, Y. Y. Wei, and S. B. Xu, *J. Geophys. Res.: Space Phys.* **125**, e2019JA027724 (2020).
- [32] T. Kotani, M. Toida, T. Moritaka, and S. Taguchi, *Geophys. Res. Lett.* **50**, e2022GL102356 (2023).
- [33] D. C. Watson and A. Bers, *Phys. Fluids* **20**, 1704 (1977).
- [34] T. Moritaka, Y. Kuramitsu, Y.-L. Liu, and S.-H. Chen, *Phys. Plasmas* **23**, 032110 (2016).
- [35] M. Toida, H. Igami, K. Saito, T. Akiyama, S. Kamio, and R. Seki, *Plasma Fusion Res.* **14**, 3401112 (2019).
- [36] T. H. Stix, *Waves in Plasmas* (Springer Science & Business Media, Cham, 1992).
- [37] C. Moser, J. LaBelle, S. Hatch, J. I. Moen, A. Spicher, T. Takahashi, C. A. Kletzing, S. Bounds, K. Oksavik, F. Sigernes, and T. K. Yeoman, *Geophys. Res. Lett.* **48**, e2020GL090747 (2021).
- [38] A. Fukuyama, H. Momota, R. Itatani, and T. Takizuka, *Phys. Rev. Lett.* **38**, 701 (1977).
- [39] C. F. F. Karney, *Phys. Fluids* **21**, 1584 (1978).
- [40] Z. Ouyang, Z. Yuan, X. Yu, and F. Yao, *Geophys. Res. Lett.* **48**, e2021GL092747 (2021).
- [41] N. A. Mecholsky, S. Akhbarifar, W. Lutze, M. Brandys, and I. L. Pegg, *Data Brief* **39**, 107508 (2021).
- [42] D. Swanson, *Plasma Waves*, 2nd ed., Series in Plasma Physics (Taylor & Francis, Oxford, UK, 2003).